Unlocking the reversible selenium electrode for non-aqueous and aqueous calcium-ion batteries

Rui Zhou, Zhen Hou, Qun Liu, Xiaoqiong Du, Jiaqiang Huang and Biao Zhang**

Rui Zhou, Zhen Hou, Qun Liu, Xiaoqiong Du, Biao Zhang

Department of Applied Physics, The Hong Kong Polytechnic University, Hung Hom, Hong Kong, China.

E-mail: biao.ap.zhang@polyu.edu.hk

Jiaqiang Huang

The Hong Kong University of Science and Technology (Guangzhou), Thrust of Sustainable Energy and Environment, Nansha, Guangzhou, 511400, Guangdong, China

E-mail: seejhuang@ust.hk

Keywords: (calcium-ion batteries, non-aqueous, aqueous, Se electrode, conversion mechanism)

Abstract: Calcium-ion batteries (CIBs) have been considered as promising multivalent ion battery systems due to the natural abundance and low redox potential of calcium. The practical realization is largely hampered by the lack of reliable electrode materials. We first explore the selenium as a new conversion-type electrode for both non-aqueous and aqueous CIBs. The selenium provides a specific capacity of 476 mAh g^{-1} with an average voltage of 2.2 V vs. Ca/Ca^{2+} at a current density of 50 mA g^{-1}, offering a higher energy density than other reported cathode materials. A long-term cyclic stability at a large current density of 500 mA g^{-1} has been achieved in non-aqueous electrolyte

through encapsulating the selenium in mesoporous carbon. The spectroscopy analysis and density functional theory calculations suggest multi-step conversion processes involving $CaSe_4$ and Ca_2Se_5 polyselenides intermediates before reaching the final CaSe phase, exhibiting a distinct reaction pathway from those in other metal-Se batteries. Furthermore, we extend the application of selenium to the aqueous electrolyte after expanding the electrochemical window. A 1.1 V-class aqueous CIB is demonstrated by coupling with a Cu-based Prussian blue electrode. The discovery of reversible Ca-Se chemistry opens new opportunities for emerging CIBs.

1. Introduction

The ever-growing energy demand has made it essential to develop efficient and readily available energy storage systems to facilitate clean energy utilization.[1] Lithium-ion batteries (LIBs) are the main power sources for portable electronics and electric vehicles. The limited reserves and uneven distribution of Li in the Earth's crust lead to concerns of resources depletion.[2] Multivalent metal-based batteries are receiving considerable attention as promising solutions because of their natural abundance.[3] Besides, their doubled or tripled electrons exchange per ion during electrochemical reaction could potentially give rise to higher volumetric/gravimetric energy densities.[4] Among them, calcium-ion batteries (CIBs) have attracted increasing interest as Ca has the closest reduction potential (-2.87 V vs. standard hydrogen electrode (SHE)) to that of Li (-3.04 V vs. SHE), enabling a high voltage for the full battery.[5] In addition, the abundance of calcium in the Earth's crust and the potential fast Ca^{2+} mobility arising

from the low charge density and polarization strength of Ca^{2+} make it attractive for designing low-cost and high-performance CIBs.[4b, 6] However, the development of CIBs is hampered by the irreversible Ca plating/stripping owing to the formation of Ca^{2+} blocking layers on Ca anode.[7] Recently, several new electrolyte systems were developed to achieve reversible Ca plating/stripping,[8] such as $Ca(BF_4)_2$ in ethylene carbonate/propylene carbonate (EC/PC),[9] $Ca(BH_4)_2$ in tetrahydrofuran (THF),[10] and $Ca[B(hfip)_4]_2$ in dimethoxy ethane (DME).[11] At the same time, efforts have been devoted to the discovery of cathodes.[12] Various materials have been reported, including layer compounds (V_2O_5,[13] α-MoO_3,[14] $VOPO_4{\cdot}2H_2O$,[15] $K_{0.5}V_2O_5$[16]), Prussian blue analogues ($KNiFe(CN)_6$,[17] $KFe[Fe(CN)_6]$,[18] $MnFe(CN)_6$),[19] transition metal oxide compounds ($Ca_3Co_2O_6$,[20] $CaMn_2O_4$[21]), polyanion compounds (NASICON-type $NaV_2(PO_4)_3$,[22] $Na_{1.5}VPO_{4.8}F_{0.7}$,[23] $NaFePO_4F$[24]) and graphite cathode wihch can store anions with high intercalation potential.[25] Besides, some exciting progress has also been made toward aqueous CIBs for reducing the fabrication cost and elevating the battery safety.[26]

Aiming at further improving the energy densities, conversion type cathodes have also been explored, with sulfur (S) as the most representative one.[27] Although the Li-S reaction shows excellent reversibility, the direct extrapolation to the Ca-S system is not successful. The initial attempt leads to a primary Ca-S battery because of the poor reversibility.[28] Assisted by the lithium-ion mediation strategy, Manthiram's group recently presents a reversible Ca-S battery for the first time.[29] Furthermore, Zhao's group reports an extraordinary rechargeable Ca-S batteries in the absence of lithium

salt, assisted by the newly developed $Ca[B(hfip)_4]_2$-based electrolyte.[12e] It delivers a superior initial capacity of 760 mAh g^{-1}, but the long-term stability remains unsatisfactory showing quick decay in 15 cycles. The inferior stability compared to Li-S system may lie in the distinct reaction pathway that has not been fully understood. Selenium (Se) in the same group as S would be a promising alternative, which shows potential advantages in the cyclic stability over S, and has been widely adopted in lithium-selenium (Li-Se), sodium-selenium (Na-Se), potassium-selenium (K-Se) and magnesium-selenium (Mg-Se) battery systems.[30] Nevertheless, to date, there is no investigation on the Se electrode for CIBs, leaving the reversibility and reaction pathway of Ca-Se elusive.

Despite the extensive studies in metal-Se reactions, a direct extrapolation would not be sufficient as the metal properties substantially affect the phase transition pathways and the associated stability. For instance, the Li-Se system undergoes a direct conversion between Se and Li_2Se without any intermediate product in carbonate electrolytes, while multi-step reaction routes are observed in Na-Se, K-Se and Mg-Se systems but showing discrete reaction pathways (Figure S1).[30g, 31] We firstly explore the reversibility and reaction mechanism of Se in CIBs by utilizing a Se/CMK-3 (ordered mesoporous carbon) composite, which is prepared via a melt-diffusion method for stabilizing the Se electrode. The Se delivers a high specific capacity of 476 mAh g^{-1} with an average potential of 2.2 V vs. Ca/Ca^{2+} in the non-aqueous electrolyte, significantly outperforming the intercalation compounds in energy density. Then, we probe the Ca-Se reaction mechanism through both experimental studies and density

functional theory (DFT) calculations, identifying several intermediate phases and the corresponding reaction potentials. Furthermore, we investigate the possibility of employing the Se electrode in an aqueous CIB. Since the reaction potential of Ca-Se is out of the electrochemical window in a normal concentration electrolyte, we effectively expand the window to 2.3 V by exploiting 6.25 M calcium bis(trifluoromethanesulfonyl)imide ($Ca(TFSI)_2$) for the successful demonstration of a revisable aqueous CIB.

2. Results and discussion

2.1. Preparation of Se electrode

We use a classic mesoporous CMK-3 carbon to accommodate Se for producing Se/CMK-3 composite electrodes to explore the intrinsic reversibility and stability of Ca-Se reactions. A facile melt-diffusion strategy is employed for the synthesis, where Se and CMK-3 are mixed and pressed into pellets before sealing in a quartz tube under a vacuum. The sample is heat-treated at 260 ^{o}C for 12 h to allow the diffusion of Se into the pores of CMK-3 host (**Figure 1**a). As shown in Figure 1b, the pristine bulk Se has a well-crystallized structure (JCDPS No. 06-0362). All characteristic peaks disappear after infiltrating Se into the CMK-3 matrix, indicating the amorphous nature of Se in the composite. The presence of Se is confirmed by X-ray photoelectron spectroscopy (XPS) analysis, presenting two peaks at 56.6 eV (Se $3d_{3/2}$) and 55.7 eV (Se $3d_{5/2}$) (Figure 1c). The thermogravimetric analysis (TGA) shows a Se content of 48 wt% (Figure 1d). The morphologies are examined by scanning electron microscopy

(SEM) and transmission electron microscopy (TEM). There is an absence of any bulk Se species on the surface of micrometer-sized rod-like CMK-3 (Figure S2 and Figure 1e), suggesting that Se is well infiltrated in the CMK-3 matrix. The corresponding elemental mappings substantiate that Se is uniformly distributed in the CMK-3 matrix (Figure 1f). No crystal lattice of Se is detected in TEM images of the composite, further verifying the amorphous Se phase (Figure 1g).

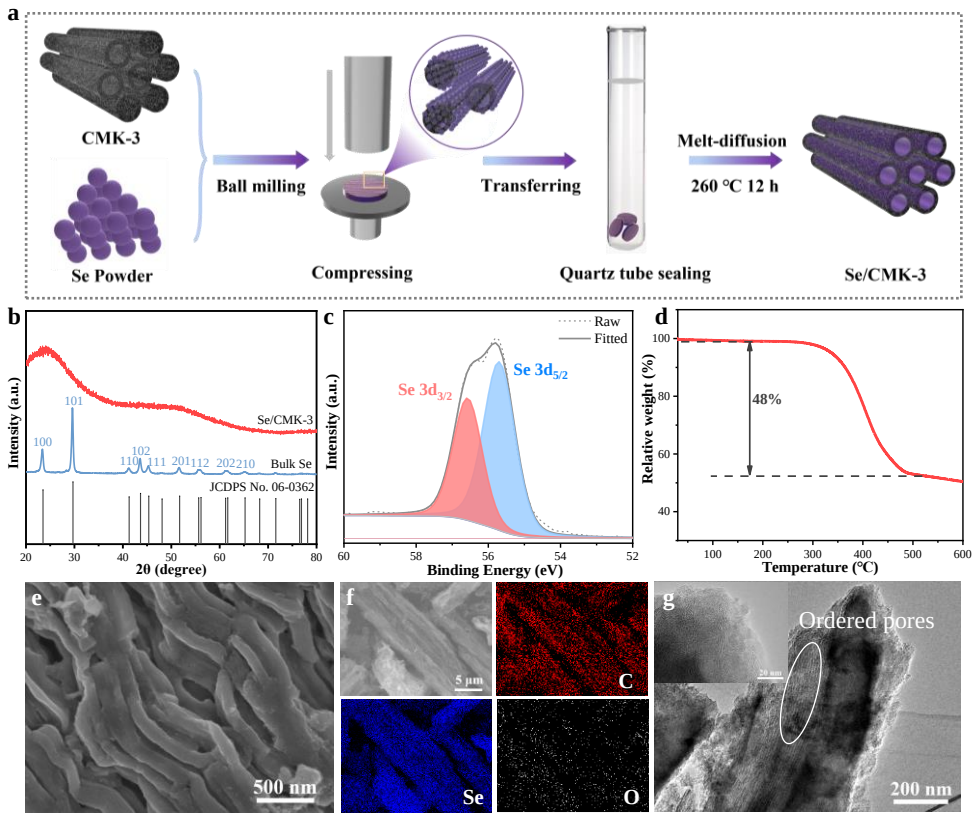

Figure 1. Synthesis process and structural characterization of Se/CMK-3 composite. a) Schematic illustration of synthesis process. b) XRD patterns of bulk Se and Se/CMK-3 composite. c) XPS spectrum of Se 3d, d) TGA curve and e, f) SEM images and elemental mappings for C, Se and O. g) TEM image and the corresponding high resolution transmission electron microscope (HRTEM) image (inset).

2.2 Reversibility of Ca-Se in organic electrolyte

To investigate the redox behavior and electrochemical performance of Ca-Se reactions in the organic electrolyte, activated carbon cloth (AC) is employed as a counter/reference electrode owing to the nearly inhibited Ca anode' plating/stripping process in most electrolytes. A classic calcium bis(trifluoromethanesulfonyl)imide in ethylene carbonate/dimethyl carbonate (0.25 M $Ca(TFSI)_2$ in EC/DMC) electrolyte is used to explore the reversibility in general systems. To better understand the electrochemical performance of Se in CIBs, the specific capacity is calculated based on the mass of Se in the electrode. As shown in **Figure 2**a and b, the discharge profiles exhibit three voltage plateaus at about -0.2, -0.75, and -1.3 V while there are also three voltage platforms at about -0.6, 0, and 0.55 V during the charging process. The observation agrees well with the CV results (Figure S3). We calibrate the redox potential of the AC reference electrode by a ferrocene/ferrocenium (Fc/Fc^+) redox couple to determine the potential of Ca-Se reactions vs. Ca/Ca^{2+} (details could be found in Figure S4). We also assemble a three-electrode Swagelok cell to simultaneously monitor the potential of working and counter electrode (Figure S5). Because of the large excess of the AC, the potential of the counter electrode only slightly deviates (< 0.1V) during the charge/discharge process (Figure S6). The average discharge voltage of Se/CMK-3 electrode is calculated to be 2.2 V vs. Ca/Ca^{2+}, which surpasses the value in the alike sustainable Na-Se (≈ 1.5 V) and K-Se (≈ 1.4 V) batteries[30d, 31c, 32] The specific capacity of Se/CMK-3 electrode suffers from a rapid decay and drops to only 96 mAh g^{-1} after 20 cycles at 100 mA g^{-1} (Figure S7). Such deterioration should be attributed to the large volume expansion of Se and loss of active materials induced by the dissolution

of polyselenides during cycling, which has been widely reported in other metal-Se batteries.[33] To improve the cyclic stability of Se/CMK-3 electrode, a free-standing carbon nanotube (CNT) interlayer is introduced between the Se/CMK-3 electrode and the separator for preventing the shuttle of dissolved species.[34] Note the neat CNTs do not directly contribute much to the capacity (Figure S8). With the assistance of CNT interlayer, a high specific capacity of 223 mAh g^{-1} is realized after 50 cycles at 100 mA g^{-1} with significantly reduced polarization (Figure S7a and S9). The voltage profiles at various cycles does not vary significantly (Figure S7b), demonstrating the similar reaction paths and decent reversibility of the Se electrode for the long-term cycles. To further investigate the effect of the CNT interlayer on the reaction kinetics. Electrochemical impedance spectroscopy is carried out at fresh cells and after 3 cycles (Figure S10). The Nyquist plots of the cells before cycling present one semicircle followed by a slope line. An equivalent circuit model in Figure S10c is employed to fit the curves, where R_e represents the electrolyte resistance, R_{ct} represents charge transfer resistance between the electrode/electrolyte interface. The cell with a CNT interlayer shows a lower R_{ct} before cycling. After cycling, a new semicircle appears in the Nyquist plots of the cells, attributed to interface contact resistance (R_p) between the cathode and polyselenides.[35] The cell with a CNT interlayer shows a greatly reduced R_p compared with that without CNT, indicating a solid capability for trapping polyselenides. The cell also shows attractive rate performance (Figure 2c), suggesting the di-valence and large size (100 pm compared to 76 pm for Li ion) of Ca ion is not an obstacle for designing high-power CIBs. Figure 2d displays long-term cycling at a higher current density of

500 mA g^{-1}: the Se/CMK-3 electrode could deliver a reversible capacity of 150 mAh g^{-1} with nearly 100% Coulombic efficiency (CE) for 300 cycles. In addition, CVs at various scan rates are conducted to evaluate the reaction kinetics of Ca-Se reaction (Figure S11). The charge is stored through the combined diffusion-controlled and psedo-capacitive behavior. The ratio of pseudo-capacitive contribution is de-coupled,[36] which increases with the growing scan rates, from 44% at 0.3 mV s^{-1} to 60% at 1 mV s^{-1}. Compared to other reported cathodes for CIBs, Se/CMK-3 electrode attains an exceptional energy density thanks to the extraordinary capacity in Ca ions uptake at a decent potential (Figure 2e and Table S1). These results indicate the Ca-Se reaction exhibits superior reversibility and stability with appropriate electrode design. A high-energy Ca-Se battery would be possible if reversible Ca metal anode could be realized, which is intensively explored in the community. Furthermore, a sample with ~75% Se is also prepared to examine the effect of active mass loading. It is a delight to observe that the cyclic capacity and stability are well maintained (Figure S12). Lastly, the cyclic performance could be further boosted by the optimization of the interlayer. Enlightened by the studies in Li-S batteries,[37] we adopt a reduced graphene oxide/CNT hybrid interlayer, which greatly alleviate the early capacity degradation (Figure S13).

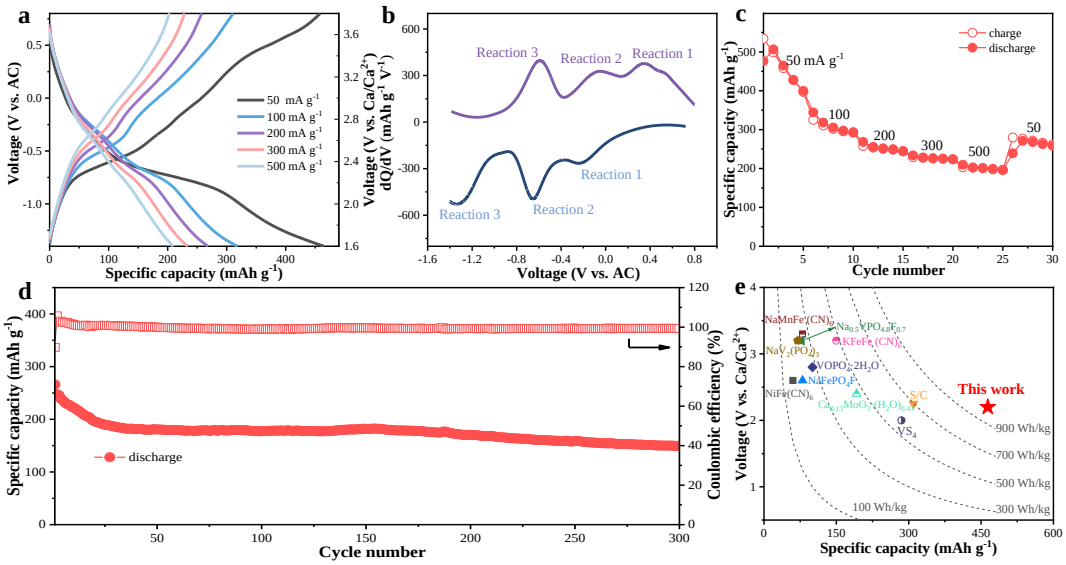

Figure 2. The electrochemical performance of Se/CMK-3 electrode. a) Voltage profiles under different current densities. b) dQ/dV curves at 30 mA g^{-1}. c) Rate performance under different current densities. d) Cycling performance at a current density of 500 mA g^{-1}. e) Comparison of specific capacity and average voltage for various reported cathodes in CIBs. The value in the 3rd cycle is adopted for all the materials to show the practically available performance.

The phase change after discharge is studied by XRD using the crystalline bulk Se considering its higher crystallinity compared to Se/CMK-3. As shown in Figure S14, the fully discharged electrode shows an amorphous structure without evident XRD peaks, which should be ascribed to the large size of the Ca^{2+} and its divalency, similar to those observed in Ca-S system.[29] To further understand the reaction mechanism of Se electrode, ex-situ Raman test for bulk Se electrode at different discharge and charge states are carried out. As shown in Figure S15, the pristine Se shows a peak at 236 cm^{-1}. During discharge, this peak becomes weaker. Another peak at about 252 cm^{-1} appears

and the intensity increases as the reaction progresses, corresponding to the gradual formation of CaSe similar to the phenomenon in the Mg-Se system.[38] In addition, a weak peak presents at about 285 cm^{-1}, which could be assigned to Se_x^{2-}. Upon charging, the CaSe and Se_x^{2-} peaks gradually fade out, accompanied by the recovery of Se peak at 236 cm^{-1}, indicating the reversible Ca-Se reactions. Therefore, we semi-quantitatively probe the chemical composition of Ca-Se reaction products by EDS (Energy dispersive spectroscope) elemental mapping of Se/CMK-3 electrode at various alloying/de-alloying stages. Ca element is uniformly distributed on the fully discharged electrode (**Figure 3**a-c). The atomic ratio of Ca and Se is 0.7 (Table S3), agreeing well with the obtained discharge capacity of 476 mAh g^{-1}. Upon charging, the electrode could be reversibly transformed back to the Se, as confirmed by the almost disappeared Ca element signals (Figure 3d-f). The 3rd discharge/charge mapping also presents a similar phenomenon (Figure S16), revealing its decent reversibility of alloying/de-alloying behavior during continuous cycling. TEM image and the corresponding EDS elemental mappings indicate the Se remains uniform distribution in CMK-3 host without apparent segregation after discharge (Figure 3g and h).

XPS analysis is carried out to unravel the discharge/charge reaction pathway of Se/CMK-3 electrode (Figure 3i). Pristine Se/CMK-3 electrode displays Se $3d_{5/2}$ and $3d_{3/2}$ peaks located respectively at 55.7 and 56.6 eV. After fully discharge, the Se 3d spectra move towards lower binding energy and could be deconvoluted into three doublet peaks. The peaks at 53.5/54.4 eV can be assigned to CaSe, and the doublet at 55.1/56.0 eV corresponds to polyselenides $CaSe_x$ ($2 \leq x \leq 8$), which indicates the Se is

converted into CaSe through multi-step reactions. These findings are consistent with the results of voltage profiles. Residue Se signal could still be detected due to the uncompleted reaction, the reason why only 0.7 Ca^{2+} per Se is uptake as inferred from the EDS mapping and reversible capacity. The existence of polyselenides is further verified by the UV-vis spectrum with an absorption peak at around 320 nm (Figure S17).[38b, 39]

Upon charging, the Se 3d peaks return to the binding energy position of pristine Se. The XPS spectra of Se/CMK-3 electrode after the 3rd cycle at discharge and charge states show a similar trend (Figure S19), proving the subsequent cycles follow the same pathway and the remarkable reversibility of Se/CMK-3 electrode. In short, the above-detailed analysis demonstrates the Se could be reversibly converted into CaSe, and its reaction path is multi-step redox transformation with the generation of intermediate $CaSe_x$ ($2 \leq x \leq 8$) products.

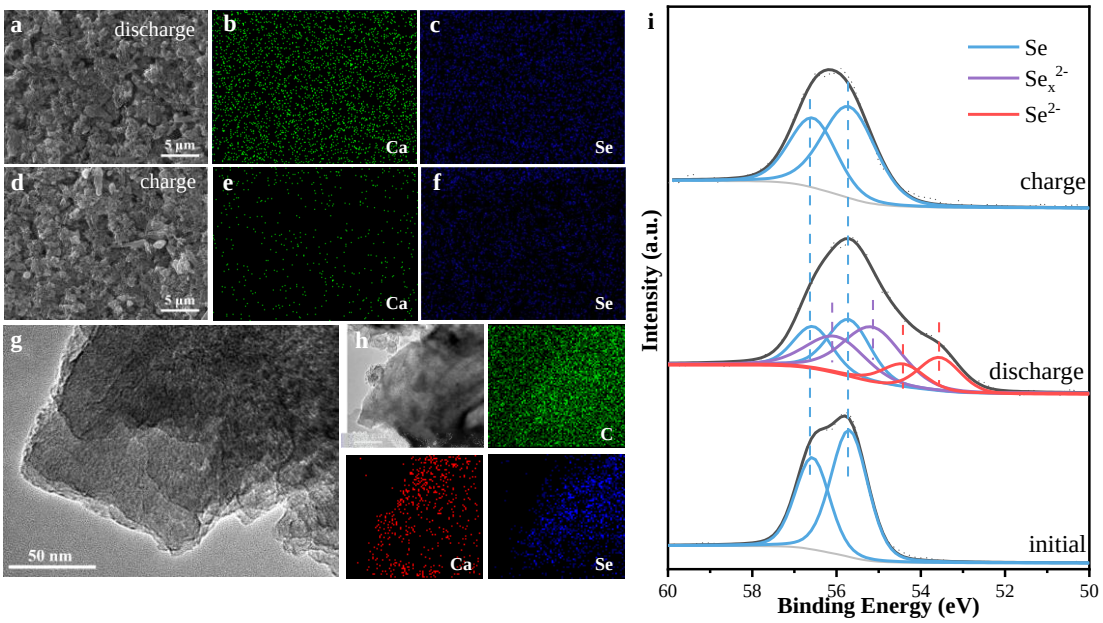

Figure 3. Analysis for the reaction mechanism of Se/CMK-3 electrode. SEM images and corresponding Ca and Se mappings a-c) after discharge and d-f) after charge. g, h) TEM images and corresponding C, Ca, and Se mappings after discharge. i) XPS Se 3d spectra at different electrochemical states.

2.3 Theoretical calculation of the reaction pathway

The experimental exploration of the detailed Ca-Se reaction pathway is restricted by the poor crystallinity of $CaSe_x$ intermediate phases. Thus, we adopt the DFT method to screen all the possible phases including those derived from the analogies in metal (Li, Na, K, Mg, and Ca)-non-metal (S, Se, and P) systems.[40] **Figure 4**a shows the formation energies of different calcium selenium compounds with varying Ca molar ratio. Among the over 50 candidates, only an intermediate phase of $CaSe_4$ is thermodynamically stable before reaching CaSe, the end-discharge product with the lowest formation energy per atom. Note that the stability of these phases is evaluated

at 0 K in the DFT calculations, which may differ from the experimental observations at room temperature (298 K). Therefore, we compare the theoretical prediction with the experimental results in Figure 4b. A good agreement of $CaSe_4$ and CaSe in the composition and reaction voltage is observed. An additional plateau at around 2.2 V appears in the experimental data but is not predicted by the convex-hull plot in Figure 4a. The most possible phase would be Ca_2Se_5 as inferred from Ca/Se atomic ratio (calculated based on the reversible capacity), and the reaction potential (vs. Ca/Ca^{2+}). The three-step conversion reaction could be further confirmed in the dQ/dV curve (Figure 2b). It shows three pairs of peaks, corresponding to the transformation of Se to triclinic $CaSe_4$ and further to orthorhombic Ca_2Se_5 until cubic CaSe during Ca ion uptake, as illustrated in Figure 4c. The detailed crystallographic structures of these three Ca-Se phases are depicted in the supplementary information (Table S4-6).

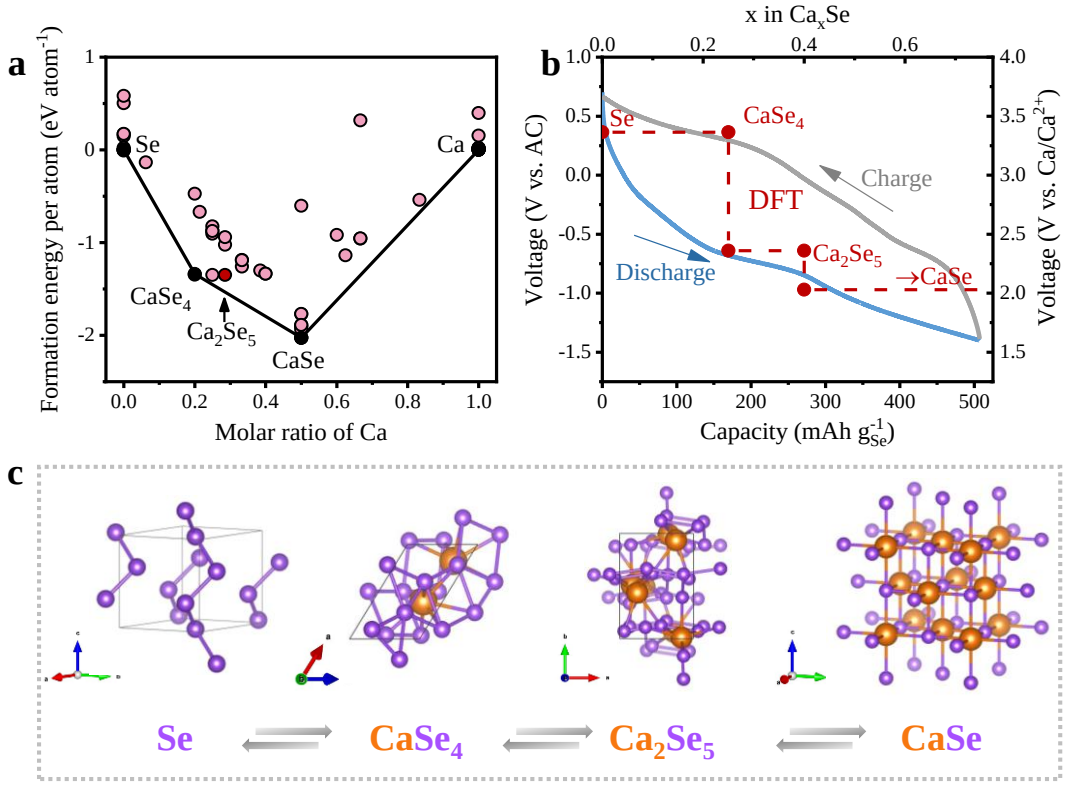

Figure 4. DFT calculations of the reaction pathway of Se cathode. a) Formation energies of predicted calcium selenides by theoretical calculations. The black points in the hull represent thermodynamically stable phases, while in the convex the red points represent the unstable phases with the purple point for the metastable Ca_2Se_5 phase. b) Computed equilibrium voltage curves and experimental curves of Se electrode. c) Computed electrochemical conversion path of Se electrode for CIBs.

2.4 Exploration in aqueous system

Considering the superior reversibility of Ca-Se reaction, we extend the research to the aqueous electrolytes for building high safety aqueous CIBs. We firstly explore the electrochemical window of 1 M $Ca(TFSI)_2$ in H_2O electrolyte (**Figure 5**a), which is too narrow to sustain the Ca-Se conversion reactions. Therefore, we expand the electrochemical window of the aqueous electrolyte by increasing the $Ca(TFSI)_2$ salt

concentration. It is found that the electrolyte with 6.25 M $Ca(TFSI)_2$ in H_2O would fulfill the stability requirement. The electrolyte has a wide electrochemical window of 2.3 V, allowing the construction of high-voltage CIBs. We first evaluate the electrochemical behavior of Se/CMK-3 electrode in the cell with AC as the counter/reference electrode. The open-circuit voltage of AC is ~0.17 V vs. saturated calomel electrode (SCE) and possesses long-term stability (Figure S20). Thus, the voltage of AC vs. Ca/Ca^{2+} is ~3.28 V in an aqueous electrolyte. The CV curve of Se/CMK-3 electrode shows two pairs of cathodic/anodic peaks (inset of Figure 5b), differing from the observations in organic system. It may related to the kinetics differences in the two electrolytes, which significantly affect the reaction pathway, as widely observed in the conversion reaction under aqueous battery.[31c] A reversible capacity of 190 mAh g^{-1} is retained after 50 cycles at 300 mA g^{-1} in the aqueous electrolyte. The capacity fading is likely to arise from the soluble short-chain $CaSe_x$ and CaSe in aqueous electrolyte, similar to the aqueous metal-S systems.[41] The reaction mechanism in the aqueous electrolyte is further investigated by XPS analysis (Figure 5c). It shows similar multi-step conversions between Se and CaSe involving the intermediate products of $CaSe_x$. SEM images and corresponding elemental mappings of Se/CMK-3 electrode after discharge and charge further prove the reversibility of the electrochemical reaction (Figure S21).

In order to certify the practical aspect of aqueous CIBs, a full cell consisting of $Ca_{0.3}[CuFe(CN)_6]_{0.66}\cdot 3.7H_2O$ ($Ca_{0.3}$CuHCF) cathode and a Se/CMK-3 anode is constructed and cycled in 6.25 M $Ca(TFSI)_2/H_2O$ electrolyte (Figure 5d). Copper

hexacyanoferrate (CuHCF) nanoparticles are synthesized by a facile co-precipitation method.[26a] The SEM image and XRD pattern (Figure S22) reveal highly crystalline nanoparticles of CuHCF, consistent with previous reports.[26a, 26c] It delivers a specific capacity of 49 mAh g^{-1} at 100 mA g^{-1} in aqueous system (Figure S23). As shown in Figure 5e, the GCD profiles of full cell have a plateau at about 1.4 V followed by a slope, giving rise to an average voltage of 1.1 V at 100 mA g^{-1}. After 50 cycles, the cell still delivers a specific capacity of 31 mAh g^{-1} based on the total mass of the active materials in the anode and cathode, corresponding to a specific energy of 34 Wh kg^{-1}. This value could be significantly boosted by exploring high-capacity and high-voltage cathodes in 6.25 M $Ca(TFSI)_2/H_2O$ electrolyte, where a 2.3 V CIB is possible when coupling with a Se anode.

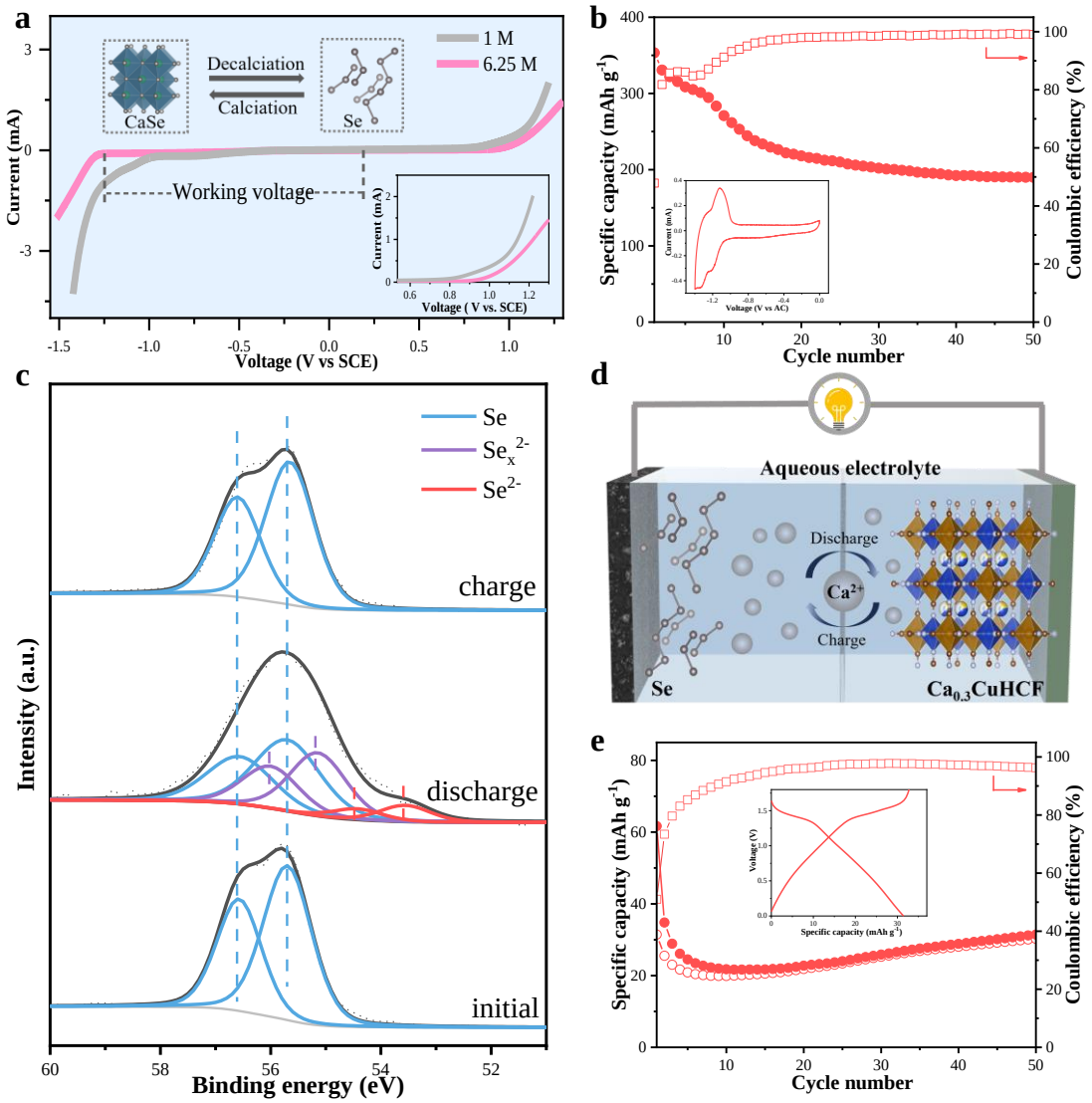

Figure 5. The electrochemical performance and reaction mechanism analysis of Se/CMK-3 electrode in an aqueous system. a) The electrochemical stability of 1 M and 6.25 M aqueous electrolytes and the voltage range of conversion reaction between Se and CaSe. b) Cycling performance at 300 mA g^{-1} and the CV curve at a scan rate of 0.3 mV s^{-1} (inset). c) XPS Se 3d spectra at different electrochemical states. d) Schematic illustration of the aqueous full cell. e) The cycling performance and voltage profiles (inset) of $Ca_{0.3}$CuHCF|Se/CMK-3 battery at a current density of 100 mA g^{-1}. The

capacity and current density are calculated based on the weight of both Se and $Ca_{0.3}$CuHCF for the full cell.

3. Conclusion

We demonstrated a new conversion-type Se electrode for CIBs through complementary theoretical and experimental studies, which is compatible with both non-aqueous and aqueous electrolytes. In a non-aqueous system, the Se/CMK-3 electrode delivers a reversible capacity of 476 mAh g^{-1} at 50 mA g^{-1} with an average CE of 99.6%. The overall performance, considering the specific capacity and average voltage, is among the best compared with reported cathode materials for CIBs. Mechanistic studies with SEM/EDS, XPS, UV-vis, and electrochemical methodologies reveal the stepwise conversion between Se^0 and Se^{2-}. Theoretical calculations indicate these intermediate phases most likely entail the $CaSe_4$ and Ca_2Se_5, whose detailed crystal structures have been unraveled for the first time. Furthermore, the Se/CMK-3 electrode also shows remarkable electrochemical activity in aqueous Ca electrolyte and exhibits a similar conversion mechanism with that in non-aqueous electrolytes. A 1.1 V-class aqueous CIB is demonstrated by coupling the Se/CMK-3 anode with a Cu-based Prussian blue cathode. This work presents an alternative direction in the exploration of high-capacity electrodes for both non-aqueous and aqueous CIBs.

4. Experimental Section

Synthesis of Se/CMK-3 composite and electrodes

In a typical synthesis, commercial selenium (Se) powder and ordered mesoporous carbon (CMK-3) with a mass ratio of 1:1 were mixed through wet ball-milling in acetone for 2 h. After evaporating acetone at room temperature, the resulting powder was pressed into a pellet and kept at 260 ℃ for 12 h in a sealed quartz tube to obtain Se/CMK-3 composite.

The slurry, consisting of Se/CMK-3, acetylene blacks, and sodium alginate binder (a mass ratio of 8:1:1) in deionized water, was cast onto a stainless steel foil and dried at 80 ℃ overnight under vacuum to fabricate Se/CMK-3 electrodes.

Characterizations

The morphologies of Se/CMK-3 were characterized by scanning electron microscopy (SEM, TESCAN MAIA3) and transmission electron microscopy (TEM, JEOL 2010F). Raman and UV-vis spectra were carried out on a Witec-Confocal Raman system (UHTS 600 SMFC VIS) with an excitation wavelength of 532 nm and a UV-vis-NIR spectrophotometer (Perkin Elmer), respectively. The Se content in Se/CMK-3 composite was analyzed by a thermogravimetric analyzer (NETZSCH, TGA, Q50). The X-ray diffraction (XRD) patterns and X-ray photoelectron spectrometry were respectively recorded on the Rigaku Smartlab X-ray diffractometer and Nexsa X-ray Photoelectron Spectrometer system.

Electrochemical measurements

CR2032 coin cells were assembled using the Se/CMK-3 as a working electrode, the commercial activated carbon cloth (AC) as a counter/reference electrode, and glass fiber membranes (GF, Whatman) as separators. 0.25 M $Ca(TFSI)_2$ in ethylene

carbonate (EC)/dimethyl carbonate (DMC) (volume ratio of 1:1) and 6.25 M $Ca(TFSI)_2$ in deionized water were respectively employed as non-aqueous and aqueous electrolytes. The electrolyte is treated with molecular sieve (4 Å), and the water content in the electrolyte is 31 ppm as measured by the Karl-Fischer method. CNT layer is also employed in aqueous system to improve the cyclic stability of Se/CMK-3 electrode. The galvanostatic charge/discharge process was carried out on a Neware battery testing system (CT-4008T). Cyclic voltammetry (CV) curves were measured using the BioLogic electrochemical workstation (VSP). To obtain the AC potential vs. Ca/Ca^{2+}, its open-circuit voltage was measured versus an Ag/Ag^{+} reference electrode[16], which is calibrated using a ferrocene/ferrocenium (Fc/Fc^{+}) redox couple (see Figure S3 for details). In an aqueous system, $Ca_{0.3}$CuHCF was prepared in two steps. First, the CuHCF electrode was fully depotassiated by charging to 0.85 V vs. AC at 50 mA g^{-1} in 0.8 M K_2SO_4 electrolyte, and was washed with DI water. The CuHCF electrode was discharged to 0V vs. AC at 50 mA g^{-1} in 6.25 M $Ca(TFSI)_2$ to obtain the $Ca_{0.3}$CuHCF electrode.

Theoretical calculations

DFT calculations were conducted by applying a projected augmented wave method [42] using generalized gradient approximation parameterized by Perdew–Burke–Ernzerhof [43] performed in the Vienna Ab initio Simulation Package.[44] We adopted an energy cutoff of 500 eV, and the k-point was selected by limiting the spacings <0.05 $Å^{-1}$. The energy and force convergence criteria were 10^{-6} eV and 0.02 eV $Å^{-1}$, respectively. We

considered the spin polarization. The equilibrium potentials were calculated according to the following equation

$$U=\frac{E_{Ca_xSe}-xE_{Ca}-E_{Se}}{-2xe} \quad (1)$$

where U is the equilibrium potential of the reaction, E_{Ca_xSe}, E_{Ca}, and E_{Se} are the computed total energies of Ca_xSe, Ca, and Se, respectively, x is the intercalation number of Ca into Se, and e is the elementary charge. Note that we selected the hexagonal phase of Se as the reference rather than the monoclinic one, because of its minor energy (0.01 eV $atom^{-1}$) above the hull and the hexagonal structure of the bulk Se in Figure 1b.

Supporting Information

Supporting Information is available from the Wiley Online Library or from the author.

Acknowledgements

Rui Zhou and Zhen Hou contributed equally to this work. This work was supported by the General Research Fund (GRF) scheme of the Hong Kong Research Grants Council (Project No. 15307221) and the Hong Kong Polytechnic University (ZVRP and 1-ZE30).

Received: ((will be filled in by the editorial staff))

Revised: ((will be filled in by the editorial staff))

Published online: ((will be filled in by the editorial staff))

References

[1] S. R. Chen, F. Dai, M. Cai, *ACS Energy Lett.* **2020**, 5, 3140.

[2] a) X. Feng, M. Ouyang, X. Liu, L. Lu, Y. Xia, X. He, *Energy Storage Mater.* **2018**,

10, 246; b) L. Lu, X. Han, J. Li, J. Hua, M. Ouyang, *J. Power Sources* **2013**, 226, 272; c) D. Lisbona, T. Snee, *Process Saf. Environ. Prot.* **2011**, 89, 434; d) A. Grimaud, *Nature Energy* **2017**, 2, 17003.

[3] Q. Liu, H. Wang, C. Jiang, Y. Tang, *Energy Storage Mater.* **2019**, 23, 566.

[4] a) X. Y. Zhang, R. J. Lv, W. J. Tang, G. J. Li, A. X. Wang, A. P. Dong, X. J. Liu, J. Y. Luo, *Adv. Funct. Mater.* **2020**, 30, 2004187; b) Y. Liang, H. Dong, D. Aurbach, Y. Yao, *Nat. Energy* **2020**, 5, 646; c) J. Xie, Q. Zhang, *Small* **2019**, 15, e1805061.

[5] a) M. E. Arroyo-de Dompablo, A. Ponrouch, P. Johansson, M. R. Palacin, *Chem. Rev.* **2020**, 120, 6331; b) C. Chen, F. Shi, Z.-L. Xu, *J. Mater. Chem. A* **2021**, 9, 11908.

[6] a) K. Ta, R. Zhang, M. Shin, R. T. Rooney, E. K. Neumann, A. A. Gewirth, *ACS Appl. Mater. Interfaces* **2019**, 11, 21536; b) B. Ji, H. He, W. Yao, Y. Tang, *Adv. Mater.* **2021**, 33, 2005501.

[7] a) I. D. Hosein, *Acs Energy Lett.* **2021**, 6, 1560; b) Y. Jie, Y. Tan, L. Li, Y. Han, S. Xu, Z. Zhao, R. Cao, X. Ren, F. Huang, Z. Lei, G. Tao, G. Zhang, S. Jiao, *Angew. Chem. Int. Ed.* **2020**, 59, 12689.

[8] a) A. Shyamsunder, L. E. Blanc, A. Assoud, L. F. Nazar, *ACS Energy Lett.* **2019**, 4, 2271; b) M. Wang, C. Jiang, S. Zhang, X. Song, Y. Tang, H. M. Cheng, *Nat. Chem.* **2018**, 10, 667.

[9] A. Ponrouch, C. Frontera, F. Bardé, M. R. Palacín, *Nat. Mater.* **2016**, 15, 169.

[10] D. Wang, X. Gao, Y. Chen, L. Jin, C. Kuss, P. G. Bruce, *Nat. Mater.* **2018**, 17, 16.

[11] Z. Li, O. Fuhr, M. Fichtner, Z. Zhao-Karger, *Energy Environ. Sci.* **2019**, 12, 3496.

[12] a) M. S. Chae, H. H. Kwak, S. T. Hong, *ACS Appl. Energy Mater.* **2020**, 3, 5107;

b) M. Cabello, F. Nacimiento, R. Alcántara, P. Lavela, C. Pérez Vicente, J. L. Tirado, *Chem. Mater.* **2018**, 30, 5853; c) C. Lee, Y.-T. Jeong, P. M. Nogales, H.-Y. Song, Y. Kim, R.-Z. Yin, S.-K. Jeong, *Electrochem. Commun.* **2019**, 98, 115; d) N. Wu, W. Yao, X. Song, G. Zhang, B. Chen, J. Yang, Y. Tang, *Adv. Energy Mater.* **2019**, 9, 1970052; e) Z. Li, B. P. Vinayan, T. Diemant, R. J. Behm, M. Fichtner, Z. Zhao‐Karger, *Small* **2020**, 16, 2001806; f) Z. Li, B. P. Vinayan, P. Jankowski, C. Njel, A. Roy, T. Vegge, J. Maibach, J. M. G. Lastra, M. Fichtner, Z. Zhao-Karger, *Angew. Chem. Int. Ed.* **2020**, 59, 11483.

[13] M. S. Chae, J. W. Heo, J. Hyoung, S.-T. Hong, *ChemNanoMat* **2020**, 6, 1049.

[14] T. Tojo, H. Tawa, N. Oshida, R. Inada, Y. Sakurai, *J. Electroanal. Chem.* **2018**, 825, 51.

[15] J. Wang, S. Tan, F. Xiong, R. Yu, P. Wu, L. Cui, Q. An, *Chem. Commun.* **2020**, 56, 3805.

[16] M. E. Purbarani, J. Hyoung, S.-T. Hong, *ACS Appl. Energy Mater.* **2021**, 4, 7487.

[17] T. Tojo, Y. Sugiura, R. Inada, Y. Sakurai, *Electrochim. Acta* **2016**, 207, 22.

[18] N. Kuperman, P. Padigi, G. Goncher, D. Evans, J. Thiebes, R. Solanki, *J. Power Sources* **2017**, 342, 414.

[19] a) T. Shiga, H. Kondo, Y. Kato, M. Inoue, *J. Phys. Chem. C* **2015**, 119, 27946; b) A. L. Lipson, B. F. Pan, S. H. Lapidus, C. Liao, J. T. Vaughey, B. J. Ingram, *Chem. Mater*. **2015**, 27, 8442; c) P. Padigi, G. Goncher, D. Evans, R. Solanki, *J. Power Sources* **2015**, 273, 460.

[20] M. Cabello, F. Nacimiento, J. R. González, G. Ortiz, R. Alcántara, P. Lavela, C. Pérez-Vicente, J. L. Tirado, *Electrochem. Commun.* **2016**, 67, 59.

[21] M. E. A.-d. Dompablo, C. Krich, J. Nava-Avendaño, N. Biškup, M. R. Palacín, F. Bardé, *Chem. Mater.* **2016**, 28, 6886.

[22] B. Jeon, J. W. Heo, J. Hyoung, H. H. Kwak, D. M. Lee, S. T. Hong, *Chem. Mater.* **2020**, 32, 8772.

[23] Z. L. Xu, J. Park, J. Wang, H. Moon, G. Yoon, J. Lim, Y. J. Ko, S. P. Cho, S. Y. Lee, K. Kang, *Nat. Commun.* **2021**, 12, 3369.

[24] A. L. Lipson, S. Kim, B. Pan, C. Liao, T. T. Fister, B. J. Ingram, *J. Power Sources* **2017**, 369, 133.

[25] J. Li, C. Han, X. Ou, Y. Tang, *Angew. Chem. Int. Ed.* **2022**, e202116668.

[26] a) S. Gheytani, Y. Liang, F. Wu, Y. Jing, H. Dong, K. K. Rao, X. Chi, F. Fang, Y. Yao, *Adv. Sci.* **2017**, 4, 1700465; b) X. Tang, D. Zhou, B. Zhang, S. Wang, P. Li, H. Liu, X. Guo, P. Jaumaux, X. Gao, Y. Fu, C. Wang, C. Wang, G. Wang, *Nat. Commun.* **2021**, 12, 2857; c) M. Adil, A. Sarkar, A. Roy, M. R. Panda, A. Nagendra, S. Mitra, *ACS Appl. Mater. Interfaces* **2020**, 12, 11489; d) R. Cang, C. Zhao, K. Ye, J. Yin, K. Zhu, J. Yan, G. Wang, D. Cao, *ChemSusChem* **2020**, 13, 3911; e) C. Han, H. Li, Y. Li, J. Zhu, C. Zhi, *Nat. Commun.* **2021**, 12, 2400; f) J. Hyoung, J. W. Heo, S.-T. Hong, *J. Power Sources* **2018**, 390, 127.

[27] a) X. Ye, J. Ruan, Y. Pang, J. Yang, Y. Liu, Y. Huang, S. Zheng, *ACS Nano* **2021**, 15, 5639; b) R. Rojaee, R. Shahbazian-Yassar, *ACS Nano* **2020**, 14, 2628; c) Y. Ji, X. Liu-Théato, Y. Xiu, S. Indris, C. Njel, J. Maibach, H. Ehrenberg, M. Fichtner, Z. Zhao-Karger, *Adv. Funct. Mater.* **2021**, 31, 2170189; d) X. Qin, J. Wu, Z.-L. Xu, W. G. Chong, J.-Q. Huang, G. Liang, B. Li, F. Kang, J.-K. Kim, *Carbon* **2019**, 141, 16.

[28] K. A. See, J. A. Gerbec, Y.-S. Jun, F. Wudl, G. D. Stucky, R. Seshadri, *Adv. Energy Mater.* **2013**, 3, 1056.

[29] X. W. Yu, M. J. Boyer, G. S. Hwang, A. Manthiram, *Adv. Energy Mater.* **2019**, 9, 1803794.

[30] a) C. P. Yang, S. Xin, Y. X. Yin, H. Ye, J. Zhang, Y. G. Guo, *Angew. Chem. Int. Ed.* **2013**, 52, 8363; b) Q. Liu, W. Deng, Y. Pan, C. F. Sun, *Chem. Sci.* **2020**, 11, 6045; c) D. Ma, Y. Li, J. Yang, H. Mi, S. Luo, L. Deng, C. Yan, P. Zhang, Z. Lin, X. Ren, J. Li, H. Zhang, *Nano Energy* **2018**, 43, 317; d) Y. Yao, M. Chen, R. Xu, S. Zeng, H. Yang, S. Ye, F. Liu, X. Wu, Y. Yu, *Adv. Mater.* **2018**, 30, 1805234; e) T. Zhang, T. Cai, W. Xing, T. Li, B. Liang, H. Hu, L. Zhao, X. Li, Z. Yan, *Energy Storage Mater.* **2021**, 41, 667; f) X. Yang, J. Wang, S. Wang, H. Wang, O. Tomanec, C. Zhi, R. Zboril, D. Y. W. Yu, A. Rogach, *ACS Nano* **2018**, 12, 7397; g) Q. Li, H. Liu, Z. Yao, J. Cheng, T. Li, Y. Li, C. Wolverton, J. Wu, V. P. Dravid, *ACS Nano* **2016**, 10, 8788.

[31] a) J. Sun, Z. Du, Y. Liu, W. Ai, K. Wang, T. Wang, H. Du, L. Liu, W. Huang, *Adv Mater* **2021**, 33, 2003845; b) A. Abouimrane, D. Dambournet, K. W. Chapman, P. J. Chupas, W. Weng, K. Amine, *J. Am. Chem. Soc.* **2012**, 134, 4505; c) R. Xu, Y. Yao, H. Wang, Y. Yuan, J. Wang, H. Yang, Y. Jiang, P. Shi, X. Wu, Z. Peng, Z. S. Wu, J. Lu, Y. Yu, *Adv. Mater.* **2020**, 32, 2003879.

[32] a) H. Wang, Y. Jiang, A. Manthiram, *Adv. Energy Mater.* **2017**, 8, 1701953; b) X. Yang, H. Wang, D. Y. W. Yu, A. L. Rogach, *Adv. Funct. Mater.* **2018**, 28, 1706609.

[33] a) X. Zhao, L. Yin, T. Zhang, M. Zhang, Z. Fang, C. Wang, Y. Wei, G. Chen, D. Zhang, Z. Sun, F. Li, *Nano Energy* **2018**, 49, 137; b) X. Hu, J. Li, G. Zhong, Y. Liu, J.

Yuan, S. Lei, H. Zhan, Z. Wen, *Small* **2020**, 16, 2005534; c) R. Muruganantham, W. R. Liu, *Chemistryselect* **2017**, 2, 8187; d) W. Hong, P. Ge, Y. Jiang, L. Yang, Y. Tian, G. Zou, X. Cao, H. Hou, X. Ji, *ACS Appl. Mater. Interfaces* **2019**, 11, 10829; e) J. Xiong, G. Cheng, G. Li, F. Qin, R. Chen, *RSC Adv.* **2011**, 1; f) X. Xu, Y. Xu, F. Xu, G. Jiang, J. Jian, H. Yu, E. Zhang, D. Shchukin, S. Kaskel, H. Wang, *J. Mater. Chem. A* **2020**, 8, 1636.

[34] a) Z. Yang, K. Zhu, Z. Dong, D. Jia, L. Jiao, *ACS Appl. Mater. Interfaces* **2019**, 11, 40069; b) Y. Zhang, Y. Guo, B. Wang, Y. Wei, P. Jing, H. Wu, Z. Dai, M. Wang, Y. Zhang, *Carbon* **2020**, 161, 413.

[35] N. Hu, X. Lv, Y. Dai, L. Fan, D. Xiong, X. Li, *ACS Appl. Mater. Interfaces* **2018**, 10, 18665.

[36] J. Wang, J. Polleux, J. Lim, B. Dunn, *J. Phys. Chem. C* **2007**, 111, 14925.

[37] J.-Q. Huang, W. G. Chong, B. Zhang, X. Ma, *Mater. Today Commun.* **2021**, 28, 102566.

[38] a) Z. Zhao-Karger, X.-M. Lin, C. Bonatto Minella, D. Wang, T. Diemant, R. J. Behm, M. Fichtner, *J. Power Sources* **2016**, 323, 213; b) Y. Zhang, M. Wang, Y. Guo, L. Huang, B. Wang, Y. Wei, P. Jing, Y. Zhang, Y. Zhang, Q. Wang, J. Sun, H. Wu, *Nanomicro Lett.* **2021**, 13, 104.

[39] D. B. Babu, K. Ramesha, *Electrochim. Acta* **2016**, 219, 295.

[40] A. Jain, S. P. Ong, G. Hautier, W. Chen, W. D. Richards, S. Dacek, S. Cholia, D. Gunter, D. Skinner, G. Ceder, K. A. Persson, *APL Mater.* **2013**, 1, 011002.

[41] a) C. Yang, L. Suo, O. Borodin, F. Wang, W. Sun, T. Gao, X. Fan, S. Hou, Z. Ma,

K. Amine, K. Xu, C. Wang, *Proc. Natl. Acad. Sci. U.S.A.* **2017**, 114, 6197; b) N. Li, Z. Weng, Y. Wang, F. Li, H.-M. Cheng, H. Zhou, *Energy Environ. Sci.* **2014**, 7, 3307.

[42] P. E. Blöchl, *Phys. Rev. B* **1994**, 50, 17953.

[43] J. P. Perdew, K. Burke, M. Ernzerhof, *Phys. Rev. Lett.* **1996**, 77, 3865.

[44] G. Kresse, J. Furthmüller, *Comput. Mater. Sci.* **1996**, 6, 15.